THE CLOSE T TAURI BINARY SYSTEM V4046 Sgr: ROTATIONALLY MODULATED X-RAY EMISSION FROM ACCRETION SHOCKS

The Astrophysical Journal, 752:100 (8pp), 2012 June 20 doi:10.1088/0004-637X/752/2/100

THE CLOSE T TAURI BINARY SYSTEM V4046 Sgr: ROTATIONALLY MODULATED X-RAY EMISSION FROM ACCRETION SHOCKS

C. Argiroffi[1,2], A. Maggio[2], T. Montmerle[3], D. P. Huenemoerder[4], E. Alecian[5], M. Audard[6,7], J. Bouvier[8], F. Damiani[2], J.-F. Donati[9], S. G. Gregory[10], M. Güdel[11], G. A. J. Hussain[12], J. H. Kastner[13], and G. G. Sacco[13]
[1] Dipartimento di Fisica, Università di Palermo, Piazza del Parlamento 1, I-90134 Palermo, Italy; argi@astropa.unipa.it
[2] INAF-Osservatorio Astronomico di Palermo, Piazza del Parlamento 1, I-90134 Palermo, Italy
[3] Institut d'Astrophysique de Paris, 98bis bd Arago, FR-75014 Paris, France
[4] MIT, Kavli Institute for Astrophysics and Space Research, 77 Massachusetts Avenue, Cambridge, MA 02139, USA
[5] Observatoire de Paris, LESIA, 5, place Jules Janssen, F-92195 Meudon Principal Cedex, France
[6] ISDC Data Center for Astrophysics, University of Geneva, Ch. d'Ecogia 16, CH-1290 Versoix, Switzerland
[7] Observatoire de Genève, University of Geneva, Ch. des Maillettes 51, CH-1290 Versoix, Switzerland
[8] UJF-Grenoble 1/CNRS-INSU, Institut de Planétologie et d'Astrophysique de Grenoble (IPAG) UMR 5274, F-38041, Grenoble, France
[9] IRAP-UMR 5277, CNRS & Université de Toulouse, 14 Av. E. Belin, F-31400 Toulouse, France
[10] Astronomy Department, California Institute of Technology, MC 249-17, Pasadena, CA 91125, USA
[11] Department of Astronomy, University of Vienna, Trkenschanzstrasse 17, A-1180 Vienna, Austria
[12] ESO, Karl-Schwarzschild-Strasse 2, D-85748 Garching bei München, Germany
[13] Center for Imaging Science, Rochester Institute of Technology, 54 Lomb Memorial Drive, Rochester, NY 14623, USA
Received 2011 May 26; accepted 2012 April 4; published 2012 May 31

ABSTRACT

We report initial results from a quasi-simultaneous X-ray/optical observing campaign targeting V4046 Sgr, a close, synchronous-rotating classical T Tauri star (CTTS) binary in which both components are actively accreting. V4046 Sgr is a strong X-ray source, with the X-rays mainly arising from high-density ($n_e \sim 10^{11}$–10^{12} cm^{-3}) plasma at temperatures of 3–4 MK. Our multi-wavelength campaign aims to simultaneously constrain the properties of this X-ray-emitting plasma, the large-scale magnetic field, and the accretion geometry. In this paper, we present key results obtained via time-resolved X-ray-grating spectra, gathered in a 360 ks *XMM-Newton* observation that covered 2.2 system rotations. We find that the emission lines produced by this high-density plasma display periodic flux variations with a measured period, 1.22 ± 0.01 d, that is precisely half that of the binary star system (2.42 d). The observed rotational modulation can be explained assuming that the high-density plasma occupies small portions of the stellar surfaces, corotating with the stars, and that the high-density plasma is not azimuthally symmetrically distributed with respect to the rotational axis of each star. These results strongly support models in which high-density, X-ray-emitting CTTS plasma is material heated in accretion shocks, located at the base of accretion flows tied to the system by magnetic field lines.

Key words: accretion, accretion disks – stars: individual (V4046 Sgr) – stars: magnetic field – stars: pre-main sequence – stars: variables: T Tauri, Herbig Ae/Be – X-rays: stars

Online-only material: color figures

1. INTRODUCTION

In the context of star formation and evolution, understanding the physics of young low-mass stars is essential. Such stars possess strong magnetic fields that regulate the transfer of mass and angular momentum to and from the circumstellar disk, via accretion and outflow phenomena. Young low-mass stars are also intense sources of high-energy emission (UV and X-rays) that ionizes, heats, and photoevaporates material in the circumstellar disk, thus affecting its physical and chemical evolution and, eventually, the disk lifetime (Ercolano et al. 2008; Gorti & Hollenbach 2009).

Low-mass pre-main-sequence stars are classified as classical T Tauri stars (CTTSs) when they still accrete mass from the circumstellar disk. They become weak-line T Tauri stars (WTTSs) when the accretion process ends. Both CTTSs and WTTSs are bright in X-rays due to the presence of hot coronal plasmas, heated and confined by the intense stellar magnetic fields (Feigelson & Montmerle 1999; Favata & Micela 2003; Preibisch et al. 2005; Güdel & Nazé 2009). It was suggested that in CTTSs also the accretion process, beside the coronal magnetic activity, can provide a further X-ray emission mechanism (Ulrich 1976; Gullbring 1994; Lamzin 1999). Magnetospheric accretion models predict that in CTTSs mass transfer from the inner disk onto the star occurs via accretion streams funneled by magnetic flux tubes (e.g., Königl 1991; Hartmann et al. 1994; Bouvier et al. 2007), where material moves in an almost free fall with typical velocities of ∼300–500 km s^{-1}. The impact with the stellar atmosphere, usually involving small fractions of the stellar surface, generates shock fronts that heat the infalling material up to temperatures of a few MK, and therefore should yield significant emission in the soft X-ray band (0.1–1 keV). Numerical modeling predicts high L_X (∼10^{30} erg s^{-1}) even for low accretion rates (10^{-10} $M_\odot$ yr^{-1}), indicating that X-ray emission related to the accretion process can rival or exceed coronal emission (Günther et al. 2007; Sacco et al. 2008) at least in principle.

Strong evidence of accretion-driven X-rays from CTTSs has been provided by the observed high densities of the X-ray-emitting plasma at $T \sim 2$–4 MK ($n_e \sim 10^{12}$–10^{13} cm^{-3}; Kastner et al. 2002; Schmitt et al. 2005; Günther et al. 2006; Argiroffi et al. 2007, 2011; Huenemoerder et al. 2007; Robrade & Schmitt 2007). These densities, considering the typical accretion rates and surface filling factors, are compatible with predictions of shock-heated material, and are significantly higher than those of typical quiescent coronal plasmas at

temperatures of a few MK ($n_e \leqslant 10^{10}$ cm^{-3}; Ness et al. 2004; Testa et al. 2004). Moreover, Güdel & Telleschi (2007) observed a soft X-ray excess in CTTSs with respect to WTTSs, compatible with the scenario of a further plasma component at a few MK produced by accretion. However, other results are discrepant with predictions: the observed L_X of the high-density cool plasma component in CTTSs is lower than that predicted from the accretion rate by more than a factor of 10 (Argiroffi et al. 2009; Curran et al. 2011), leaving the coronal component the major contributor to the X-ray emission in CTTSs; furthermore in the cool plasma of CTTSs the density increases for increasing temperature, at odds with predictions based on a single accretion stream (Brickhouse et al. 2010). Because of these apparent discrepancies different scenarios were proposed, suggesting that the high-density cool plasma in CTTSs could be coronal plasma, confined into magnetic loops, that is somehow modified by the accretion process (Güdel et al. 2007; Brickhouse et al. 2010; Dupree et al. 2012).

In addition to containing plasma at a few MK, the shock region is known to be associated with material at $T \sim 10^4$ K or more, significantly hotter than the surrounding unperturbed photosphere, as a consequence of the energy locally deposited by the accretion process. This photospheric hot spot produces excess emission in the UV and optical bands, which is often rotationally modulated because of the very small filling factor of the accretion-shock region and because accretion streams are usually not symmetric with respect to the rotation axis (Bouvier et al. 1993; Herbst et al. 1994; Petrov et al. 2001). Therefore, if the observed high-density X-ray-emitting plasma also originates in the accretion shock, then its X-ray emission might display rotational modulation. Specifically, plasma heated in the accretion shock, observed in the X-rays, could display periodic variations in density, emission measure, average temperature, absorption, and source optical depth, as a consequence of stellar rotation. First hints of accretion-driven X-rays that vary because of the stellar rotation were provided by Argiroffi et al. (2011) for the star V2129 Oph.

Understanding the origin of this high-density plasma is important, both for constraining the total amount of X-rays emitted in CTTSs, and setting the energy balance of the accretion-shock region (Sacco et al. 2010). Eventually, a definitive confirmation that this plasma component is material heated in the accretion shock would make its X-ray radiation an insightful tool to probe the physical properties (i.e., density and velocity) of the accretion stream, and to measure the chemical composition of the inner disk material (Drake et al. 2005).

To search for such X-ray modulation effects, we planned and carried out X-ray monitoring of V4046 Sgr, a close binary CTTS system in which both components are actively accreting from a circumbinary disk (see Section 3).

In this work, we describe the first results from an *XMM-Newton* Large Program focused on V4046 Sgr, based on time-resolved high-resolution X-ray spectroscopy on timescales down to 1/10 of the system orbital period. To constrain the large-scale magnetic field and the accretion geometry, we also carried out a coordinated multi-wavelength campaign involving photometry, spectroscopy, and spectropolarimetry of V4046 Sgr.

In Section 2, we summarize the project focused on V4046 Sgr, whose properties are described in Section 3. Details of the data processing and analysis are reported in Section 4. The observing results are presented in Section 5, and then discussed in Section 6.

2. THE V4046 Sgr PROJECT

The *XMM-Newton* observation of V4046 Sgr consists of a 360 ks exposure performed on 2009 September 15–19 (ObsIDs: 0604860201, 0604860301, and 0604860401). This observation is part of a quasi-simultaneous multi-wavelength campaign (optical photometry with REM/ROSS, 2009 September 1–30; optical spectroscopy with TNG/SARG, 2009 September 10–17; optical spectropolarimetry with CFHT/ESPADONS, 2009 September 2–8) aimed at studying simultaneously the properties of coronal plasmas, stellar magnetic field structure, photospheric spots (both cool spots and hot spots), and the accretion process.

Here, we present the results obtained with the *XMM-Newton*/Reflection Grating Spectrometers (RGS) specifically aimed at searching for rotational modulation in the accretion-driven X-rays. The results of the entire observing campaign are presented in a series of papers describing, among other results, the properties of the X-ray-emitting plasma (A. Maggio et al., in preparation), maps of the large-scale magnetic field structure and accretion geometry as inferred from optical spectropolarimetry (Donati et al. 2011; G. A. J. Hussain et al., in preparation; S. G. Gregory et al., in preparation), variations in the accretion process over a range of timescales (G. G. Sacco et al., in preparation), and detection and identification of a distant comoving WTTS system (Kastner et al. 2011).

3. V4046 Sgr PROPERTIES

V4046 Sgr is a close CTTS binary system composed of two stars of solar-like mass (masses of 0.91 and 0.88 $M_\odot$, radii of 1.12 and 1.04 $R_\odot$; Donati et al. 2011), separated by 8.8 $R_\odot$. The two components are synchronously rotating with a period of 2.42 d, in circularized orbits (Stempels & Gahm 2004). V4046 Sgr is estimated to lie at a distance of 73 pc (Torres et al. 2008) and it is viewed with an inclination of 35° (the angle between the rotation axis and the line of sight; Stempels & Gahm 2004; Kastner et al. 2008), with the orbital axis of the binary likely aligned with the individual stellar rotation axes (Donati et al. 2011). At an age of ∼10–15 Myr (Torres et al. 2008; Donati et al. 2011) and classified as a CTTS, V4046 Sgr is still surrounded by a dusty, molecule-rich circumbinary disk (Rodriguez et al. 2010) from which both the components are actively accreting (Stempels & Gahm 2004).

A previous *Chandra* observation (Günther et al. 2006) showed that V4046 Sgr has a cool plasma component ($T \approx$ 2–4 MK) at high density ($n_e \approx (0.3\text{–}1) \times 10^{12}$ cm^{-3}), interpreted as material heated in the accretion shock.

At the time of the *XMM-Newton* observation, the spectroscopic optical monitoring demonstrated that both components were accreting with a constant rate of 5×10^{-10} $M_\odot$ yr^{-1} (inferred from the analysis of the Ca II IRT; Donati et al. 2011). Both components displayed complex magnetic fields (average surface intensity of ∼200 G; Donati et al. 2011), significantly weaker than that of younger solar-like CTTSs (e.g., Donati et al. 2010). These magnetic fields are not strong enough to disrupt local disks farther than 1 $R_\star$ above the stellar surface; thus the formation of circumstellar disks around each component, distinct from the circumbinary disk, may be possible (de Val-Borro et al. 2011). The accretion process, based on Ca II IRT, did not show significant rotational modulation, suggesting that post-shock material contributing to these lines is symmetrically distributed with respect to the stellar poles.

Table 1
Observed Line Fluxes at Different Time Intervals

	Rot. Phase	Ne X 12.13 Å 6.3 MK	Ne IX 13.45 Å 4.0 MK	Ne IX 13.55 Å 3.5 MK	Ne IX 13.70 Å 4.0 MK	Fe XVII 15.02 Å 5.6 MK	O VIII 16.01 Å 3.2 MK	O VIII 18.97 Å 3.2 MK	O VII 21.60 Å 2.0 MK	N VII 24.78 Å 2.0 MK
$F_{int1/seg1}$	0.67	34.0 ± 5.2	58.3 ± 6.6	21.1 ± 5.2	21.3 ± 4.8	14.9 ± 3.2	15.3 ± 3.3	90.6 ± 8.9	18.9 ± 8.9	67.6 ± 9.4
$F_{int2/seg1}$	0.79	33.0 ± 5.0	76.0 ± 7.0	17.7 ± 5.1	16.8 ± 4.3	7.4 ± 3.0	12.8 ± 3.7	81.8 ± 8.1	17.0 ± 9.3	69.5 ± 9.4
$F_{int3/seg1}$	0.91	31.7 ± 4.7	56.1 ± 6.9	34.3 ± 6.2	25.3 ± 5.5	14.0 ± 3.2	17.6 ± 3.7	101.0 ± 9.1	42.5 ± 11.7	89.9 ± 11.0
$F_{int4/seg1}$	0.03	45.9 ± 5.4	65.7 ± 6.9	31.6 ± 5.8	24.9 ± 4.9	10.5 ± 3.3	9.8 ± 3.3	118.2 ± 9.7	48.3 ± 11.0	62.3 ± 9.2
$F_{int5/seg1}$	0.15	40.9 ± 6.6	59.8 ± 8.3	22.0 ± 6.8	27.1 ± 6.3	11.6 ± 3.6	22.3 ± 5.0	52.4 ± 8.9	30.6 ± 12.7	52.3 ± 10.8
$F_{int1/seg2}$	0.50	40.2 ± 5.2	71.0 ± 7.4	33.8 ± 6.1	37.3 ± 5.6	14.5 ± 3.4	10.9 ± 3.7	95.6 ± 8.4	33.2 ± 11.8	119.1 ± 10.7
$F_{int2/seg2}$	0.62	54.3 ± 5.5	37.7 ± 6.1	30.3 ± 5.7	35.9 ± 5.3	16.9 ± 3.6	13.1 ± 3.7	92.0 ± 8.5	31.2 ± 10.1	64.3 ± 9.3
$F_{int3/seg2}$	0.73	45.6 ± 5.5	43.1 ± 6.3	45.4 ± 6.2	20.2 ± 4.9	18.5 ± 3.7	20.4 ± 4.0	101.9 ± 8.4	19.0 ± 7.2	72.5 ± 9.5
$F_{int4/seg2}$	0.85	42.5 ± 5.2	55.4 ± 6.6	31.7 ± 6.0	29.5 ± 5.3	17.4 ± 3.4	10.6 ± 3.4	112.6 ± 9.4	42.6 ± 9.6	77.0 ± 10.4
$F_{int5/seg2}$	0.97	42.6 ± 5.7	75.1 ± 8.2	60.8 ± 7.5	39.7 ± 6.1	5.2 ± 2.8	18.8 ± 3.7	121.3 ± 9.6	24.1 ± 9.7	107.4 ± 11.6
$F_{int1/seg3}$	0.32	61.6 ± 6.0	46.3 ± 6.0	26.6 ± 5.4	20.7 ± 4.6	5.8 ± 3.4	9.7 ± 3.7	135.8 ± 9.8	35.0 ± 9.1	69.4 ± 10.0
$F_{int2/seg3}$	0.44	48.3 ± 5.6	68.5 ± 7.2	41.3 ± 6.2	32.5 ± 5.1	14.7 ± 3.7	12.8 ± 3.7	98.3 ± 8.7	53.3 ± 12.3	76.7 ± 10.0
$F_{int3/seg3}$	0.56	43.3 ± 5.3	66.6 ± 7.1	20.4 ± 5.3	35.9 ± 5.1	15.1 ± 3.4	16.6 ± 3.9	112.0 ± 9.1	39.9 ± 10.4	94.6 ± 10.9
$F_{int4/seg3}$	0.68	23.7 ± 4.3	36.9 ± 5.9	9.9 ± 4.3	30.7 ± 5.1	4.7 ± 3.0	11.9 ± 3.1	69.6 ± 7.7	24.9 ± 9.9	43.4 ± 7.8
$F_{int5/seg3}$	0.79	39.1 ± 5.8	41.9 ± 6.4	21.4 ± 6.1	20.7 ± 4.9	13.8 ± 3.5	13.7 ± 3.7	75.0 ± 8.9	26.0 ± 11.9	56.4 ± 10.0

Notes. For each line, the table head reports: ion, wavelength, and maximum formation temperature. $F_{int i/seg j}$ refers to the line fluxes measured in the ith interval of the jth observing segment. For each time interval, the listed phase corresponds to the central time of the bin. Line fluxes are in 10^{-6} photons s^{-1} cm^{-2}. Errors correspond to 1σ.

The optical monitoring campaign confirmed the orbital/rotational period (2.42 d), and determined the conjunction and quadrature epochs at the time of the *XMM-Newton* observation.[14] In this work, we adopt the phase reference defined in Stempels & Gahm (2004, HJD = 2446998.335 + 2.4213459 E, with phase 0.0 indicating the quadrature with primary receding). However, our optical monitoring revealed a phase shift of 0.069 with respect to that ephemeris, with quadratures occurring at phases 0.93 and 0.43, and conjunctions at phases 0.18 and 0.68 (Donati et al. 2011).

4. OBSERVATIONS

The *XMM-Newton* observation of V4046 Sgr, composed of three observing segments of ∼120 ks each separated by gaps of ∼50 ks, covered 2.2 system rotations. X-ray-emitting material heated in the accretion shock is expected to have temperatures of a few MK at most. Therefore, to search for X-ray variability possibly produced in the accretion shock we analyzed the *XMM-Newton*/RGS spectra that contain emission lines that specially probe the coolest plasma components.

The RGS spectrograph, composed of two nominally identical gratings (RGS1 and RGS2), covers the ∼2–38 Å wavelength range. The first-order spectrum, embracing the 4–38 Å band, has a resolution FWHM of 0.06 Å, while the second-order spectrum provides a resolution FWHM of 0.03 Å in the ∼2–19 Å range. We extracted RGS spectra using the standard RGSPROC task. Data were filtered discarding time segments affected by high background count rates. The final net exposures of the three observing segments were of 115, 122, and 120 ks, respectively. We then applied the RGSCOMBINE task to add the RGS1 and RGS2 spectra of the same order. In total, 34,800 and 8200 net counts were registered in the first- and second-order RGS spectra, respectively.

We analyzed the RGS spectra using the IDL package PINTofALE v2.0 (Kashyap & Drake 2000) and the XSPEC v12.5 (Arnaud 1996) software. We measured individual line fluxes by fitting first- and second-order[15] RGS spectra simultaneously. The fit procedure was performed in small wavelength intervals ($\Delta\lambda \lesssim 1.0$ Å). The adopted best-fit function takes into account the RGS line spread function (determined by the matrix response function) and the continuum contribution (determined by adding a constant to the line emission, and leaving this constant as a free parameter in the fit).

5. RESULTS

The RGS spectra collected during the entire observation (see details in A. Maggio et al., in preparation) indicate that the main properties of the X-ray-emitting plasma of V4046 Sgr are similar to those observed during the previous *Chandra* observation (Günther et al. 2006): the plasma at $T \sim$ 1–4 MK has high density, $n_e \sim 10^{11}$–10^{12} cm^{-3}, as determined by the f/i line ratio of He-like triplets of N VI, O VII, and Ne IX.[16]

5.1. Time-resolved RGS Spectra

To investigate variability on short timescales, we analyzed RGS spectra gathered in time intervals of ∼25 ks (i.e., bins of 0.12 in rotational phase). In total nine lines have fluxes detected at the 1σ level in all the time intervals. These lines, and their fluxes at different time intervals, are reported in Table 1. Significant variability on the timescales explored is observed for all the lines listed.

To check for variations in the coolest plasma components, we considered lines with peak formation temperature $T_{max} < 5$ MK among the lines reported in Table 1. This sample of lines, named *cool* lines, is composed of the Ne IX triplet (13.45, 13.55, and 13.70 Å), O VIII Lyβ[17] and Lyα (16.00 and 18.98 Å), O VII resonance line (21.60 Å), and N VII Lyα (24.78 Å). Among the lines reported in Table 1, the Ne X and Fe XVII lines stay out of

[14] The quadrature with primary receding occurred at 2455078.199 HJD.

[15] Second-order spectrum was used only for lines contained in its wavelength range.

[16] The measurements of the Ne IX triplet were performed by including in the fit the Fe XIX line at 13.52 Å, that is anyhow weaker than the Ne IX lines.

[17] This is blended with an Fe XVIII, that is however negligible because of the emission measure distribution and abundances of the X-ray-emitting plasma.

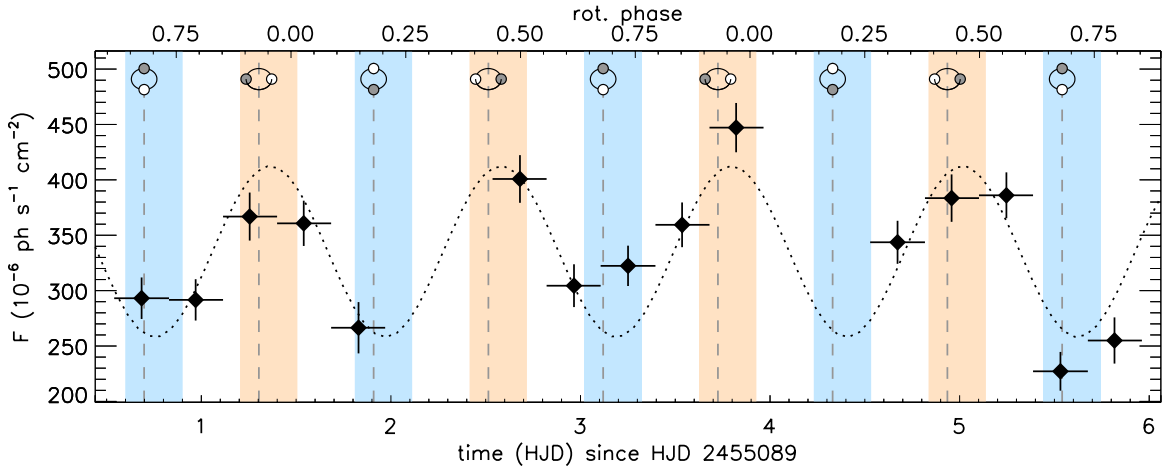

Figure 1. Total flux of the cool line set vs. time. The set of cool lines is composed of the Ne IX triplet (13.45, 13.55, and 13.70 Å), O VIII Lyα and Lyβ (16.00 and 18.98 Å), O VII resonance line (21.60 Å), and N VII Lyα (24.78 Å). Horizontal error bars represent the time-bin width. The dotted line marks the best-fit sinusoidal function. Orbital/rotational phases are computed according to the ephemeris HJD = 2446998.335 + 2.4213459 E defined in Stempels & Gahm (2004). Vertical dashed lines (dark gray) indicate quadrature and conjunction epochs, with the corresponding schematic views of the system plotted above (white and gray circles represent the primary and secondary components, respectively). Time intervals adopted for extracting spectra corresponding to *low* and *high* phases are marked by the vertical bands (light blue and light red for the low and high phases, respectively).

(A color version of this figure is available in the online journal.)

Table 2
Best-fit Parameters

Set Name	Line Set	P[a] (days)	A[b] (%)	t_{max}[c] (days)	$(\chi^2_{red,1})$[d]	$(\chi^2_{red,2})$[e]
Cool lines	Ne IX+O VIII+O VII+N VII	1.22 ± 0.01	23 ± 2	1.36 ± 0.05	2.91	8.93
Cool line subset	O VIII+O VII+N VII	1.21 ± 0.02	22 ± 3	1.35 ± 0.06	2.31	5.50
Cool line subset	O VII+N VII	1.22 ± 0.03	30 ± 5	1.30 ± 0.05	0.65	2.89
Cool line subset	Ne IX	1.22 ± 0.02	25 ± 4	1.40 ± 0.06	2.33	5.12
Hot lines	Ne X+Fe XVII	1.12 ± 0.03	14 ± 5	1.61 ± 0.10	3.63	3.46

Notes.
[a] Period.
[b] Amplitude.
[c] First epoch of maximum flux after observation starts, since HJD 2455089.
[d] Reduced χ^2 obtained with a sinusoid as best-fit function (four free parameters).
[e] Reduced χ^2 obtained with a constant as best-fit function (one free parameter).

the *cool* line sample, because their T_{max} is higher than 5 MK. Therefore, their flux likely includes significant contributions from hot plasma. These two lines compose the *hot* line sample.

To maximize the signal-to-noise ratio of the coolest plasma emission, we added the measured fluxes of the cool lines for each time interval. This total line flux, plotted in Figure 1, is variable and the observed modulation is clearly linked to the stellar rotation: the flux is higher near phases 0.0 and 0.5, i.e., quadrature phases, and lower near phases 0.25 and 0.75, i.e., conjunction phases. To confirm this variability pattern, we fitted these observed flux variations with a sinusoid plus a constant. We left all the best-fit function parameters (period, phase, amplitude, and the additive constant) free to vary. We obtained a best-fit period of 1.22 ± 0.01 d and an amplitude of $23\% \pm 2\%$ with respect to the mean value (Table 2). The inferred period is exactly half the rotational period of the system. As guessed, maximum and minimum phases occur approximately at quadrature and conjunction, respectively. To check whether this observed modulation is effectively linked to the cool plasma emission, and not to a given line emission, we performed the same fit by separately considering the total flux obtained from different and independent cool line subsets. In all the cases inspected (see Table 2), we found the same periodic variability (period, phase, amplitude).

We checked whether this modulation is present also in the emission of hotter plasma by applying the same fit procedure to the total flux of the hot lines, Ne X and Fe XVII. Fit results are reported in Table 2; in this case the periodic modulation is not detected. The observed variability is instead likely dominated by hot (coronal) plasma. Figure 2 shows a comparison between Ne X+Fe XVII line variability with modulation observed for the cool lines. The detected X-ray rotational modulation is also not visible in the EPIC light curves (A. Maggio et al., in preparation), even considering only a soft band. The substantial continuum contribution mostly due to the highly variable hot plasma likely masks the rotationally modulated signal. Hence, we conclude that the observed X-ray line flux modulation is due to the high-density, cool plasma component.

To understand the nature of the observed variability, we searched for variations in the average temperature by considering ratios of lines originating from the same element. All the ratios inspected display significant variability, but are not correlated among themselves, and are not related to the rotational phase. We also searched for variations in the plasma density,

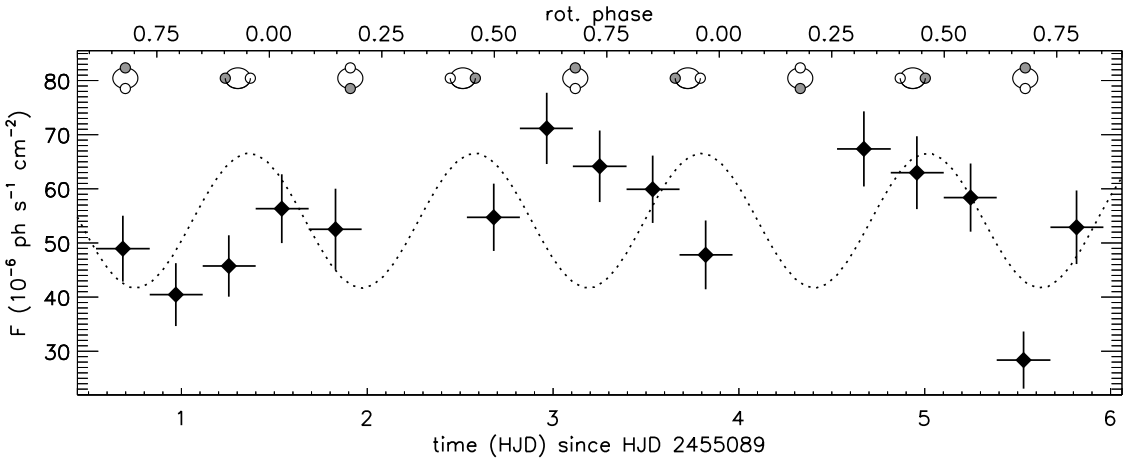

Figure 2. Total flux of the hot line set vs. time. The set of hot lines is composed of the Ne X Lyα line at 12.13 Å and Fe XVII line at 15.02 Å. The dotted line marks a sinusoidal function with the same period, phase, and relative amplitude obtained from the best fit of the total flux of the cool line set. The hot lines do not show rotational modulation, unlike the cool lines, see Figure 1, suggesting that their variability is associated with coronal plasma variability.

Table 3
Observed Line Fluxes at Different Phases

Ion	λ (Å)	T_{max} (MK)	F_{Low} (10^{-6} photons s^{-1} cm^{-2})	F_{High} (10^{-6} photons s^{-1} cm^{-2})
Ne X	10.24	6.3	5.9 ± 1.3	4.1 ± 1.2
Ne IX	11.55	4.0	4.1 ± 1.6	11.9 ± 2.1
Ne X	12.13	6.3	46.2 ± 3.0	50.6 ± 3.0
Fe XXI	12.28	10.0	4.3 ± 1.6	3.7 ± 1.8
Ne IX	13.45	4.0	72.2 ± 4.0	75.3 ± 3.9
Fe XIX	13.52	10.0	16.3 ± 3.3	9.4 ± 3.3
Ne IX	13.55	3.5	27.3 ± 3.1	49.4 ± 3.5
Ne IX	13.70	4.0	29.9 ± 2.9	41.7 ± 3.1
Fe XVIII	14.20	7.9	5.1 ± 1.6	3.8 ± 1.5
Fe XVII	15.02	5.6	13.6 ± 1.8	14.3 ± 1.9
O VIII	15.18	3.2	4.3 ± 1.7	7.9 ± 1.8
O VIII	16.01	3.2	19.5 ± 2.1	16.2 ± 2.0
Fe XVII	16.78	5.0	11.4 ± 2.1	10.3 ± 1.9
Fe XVII	17.05	5.0	12.7 ± 2.4	14.1 ± 2.4
Fe XVII	17.10	5.0	5.8 ± 2.6	8.9 ± 2.6
O VIII	18.97	3.2	90.5 ± 4.7	113.9 ± 4.8
N VII	20.91	2.2	11.0 ± 3.1	7.0 ± 2.9
O VII	21.60	2.0	24.8 ± 4.0	46.0 ± 6.1
O VII	21.81	2.0	17.3 ± 5.9	24.4 ± 6.3
O VII	22.10	2.0	12.2 ± 3.9	10.3 ± 3.3
N VII	24.78	2.0	72.0 ± 5.4	106.6 ± 6.0
N VI	28.79	1.6	25.0 ± 4.5	17.9 ± 4.5
N VI	29.08	1.3	12.7 ± 4.1	7.5 ± 3.9
C VI	33.73	1.6	25.3 ± 5.2	35.6 ± 5.7

Notes. Line fluxes measured during the *high* and *low* phases are listed. Flux errors correspond to 1σ.

Table 4
Line Flux Ratios at Different Phases

Line Flux Ratio	R_{Low}	R_{High}
Ne IX (13.45 Å)/Ne IX (11.55 Å)	18^{+11}_{-5}	$6.4^{+1.4}_{-1.0}$
O VIII Lα (18.97 Å)/O VIII Lyβ (16.01 Å)	$4.6^{+0.6}_{-0.5}$	$7.0^{+1.1}_{-0.8}$
N VII Lα (24.78 Å)/N VII Lyβ (20.91 Å)	$6.5^{+2.6}_{-1.5}$	15^{+11}_{-5}

Note. Ratio errors correspond to the 68% confidence level.

probed by the f/i ratio of the Ne IX triplet. This line ratio is approximately constant ($f/i \approx 1$, indicating $n_e \approx 10^{12}$ cm^{-3}) during the entire observation, except for a lower value measured during the third interval of the second segment ($f/i = 0.45 \pm 0.13$, corresponding to $n = (5.2^{+2.0}_{-1.3}) \times 10^{12}$ cm^{-3}), and a higher value observed during the fourth interval of the third segment ($f/i = 3^{+2.5}_{-1.1}$, corresponding to $n < 4 \times 10^{11}$ cm^{-3}). These variations appear to be associated with episodic events, like clumpy accretion flows, and not with a rotational modulation effect.

5.2. RGS Spectra at Different Phases

The total flux of the cool lines from V4046 Sgr displayed variations in time linked to the stellar rotation. To investigate the differences in the X-ray-emitting plasma corresponding to epochs of low and high fluxes of the cool lines, we added RGS data collected at the same phases with respect to the X-ray rotational modulation. We extracted two RGS spectra obtained by adding all the events registered during time intervals centered on maximum and minimum times, with duration of one-fourth of the observed X-ray period (integration time intervals are shown in Figure 1). The two resulting *low* and *high* spectra, whose exposure times are 84 and 94 ks, respectively, are shown in Figure 3, while the measured line fluxes, detected at the 1σ level in the two spectra, are listed in Table 3.

We searched for differences in the *low* and *high* spectra to investigate how the emitting plasma properties vary between these two phases. The two spectra display significantly different photon flux ratios of N VII, O VIII, and Ne IX lines, as reported in Table 4. In principle, these line ratios may vary due to changes of absorption, plasma temperature, or source optical depth. In Figure 4, we plot the measured line ratios together with the values predicted in the optically thin regime for different temperatures and different hydrogen column densities, N_H.

Absorption can change line ratios because, on average, lines at longer wavelengths suffer larger attenuation for increasing N_H. The two N VII lines considered here are an exception, because the absorption cross-section of the interstellar medium has the oxygen K-shell edge (23.3 Å, e.g., Wilms et al. 2000) located between their wavelengths, making the longer wavelength line, the Lyα (24.78 Å), slightly less absorbed than the Lyβ (20.91 Å). The two lines however suffer very similar absorption, making the absorption effect of little relevance in the case of the N VII Lyα/Lyβ ratio (as can be seen from the upper panel of Figure 4, where the curves predicted for different N_H are very similar). Therefore, any change in this line ratio, as that observed, is hardly explained in terms of N_H variability.

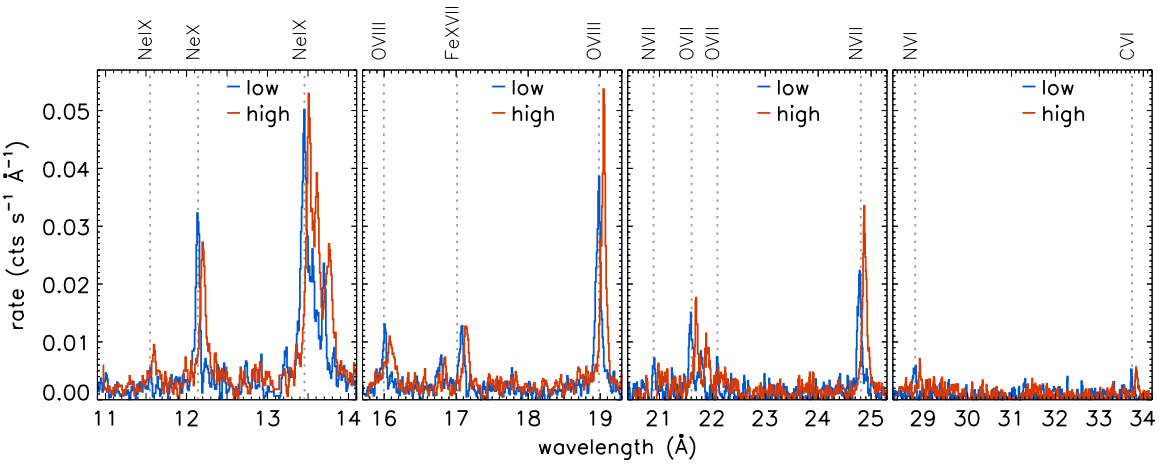

Figure 3. RGS spectra corresponding to minimum (*low*) and maximum (*high*) phases, corresponding to exposure times of 84 and 94 ks, respectively. For clarity reasons the two spectra are slightly smoothed, and the spectrum of the high-flux phase is shifted toward longer wavelengths by 0.1 Å.

(A color version of this figure is available in the online journal.)

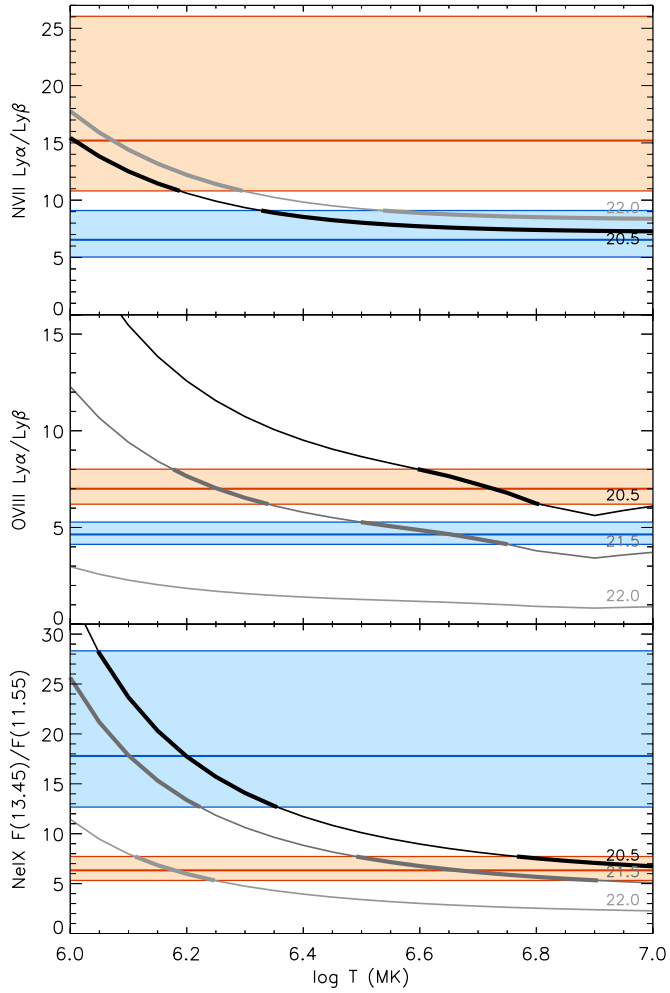

Figure 4. Lyα to Lyβ photon flux ratio for the N VII and O VIII H-like ions and 13.45 Å to 11.55 Å for the Ne IX He-like ion vs. plasma temperature. Horizontal bands indicate values measured during *high* (red) and *low* (blue) phases. Black, dark gray, and light gray lines represent predicted values for different absorptions $N_{\rm H}$, with labels reporting the corresponding log $N_{\rm H}$ value, and with thicker lines marking curve portions compatible with the observed ratios.

(A color version of this figure is available in the online journal.)

Instead, an $N_{\rm H}$ decrease from the *low* to the *high* state might explain the variation of the O VIII line ratios, but an opposite $N_{\rm H}$ variation should be invoked to justify the Ne IX variability (middle and lower panels of Figure 4). All these findings indicate that the hydrogen column density toward the source appears to be unchanged, and that the line ratio variability is produced by a different mechanism. This conclusion is supported by the similar fluxes between *low* and *high* spectra measured for the two lines at long wavelengths (N VI at 28.8 Å and C VI at 33.7 Å), the most affected by absorption, and it is also confirmed by the fully-fledged analysis of the EPIC data presented in A. Maggio et al. (in preparation), where $N_{\rm H}$ is found to vary by only a factor two over the whole observation around a mean value of 3×10^{20} cm^{-2} (i.e., log $N_{\rm H} = 20.5$).

The three ratios explored depend also on temperature, because of the different energy of the upper levels of the two electronic transitions considered in each ratio. In this respect, the three ratios do not vary consistently. In fact, a temperature decrease from the *low* state to the *high* state could explain the increasing N VII and O VIII line ratios, but not the variation in Ne IX lines. The derivation of the plasma model (see A. Maggio et al., in preparation) is beyond the scope of this work, but we anticipate here that the emission measure distribution does not appear to vary enough between the two phases to justify the observed variations of the line ratios. Moreover, the average plasma temperature (log $T \sim 6.6$–6.7), together with the measured $N_{\rm H}$, indicates that, in some phases, line ratios are not compatible with the optically thin limit, irrespective of the nature of their variability.

Optical depth effects can change line ratios because each line optical depth is directly proportional to the oscillator strength of the transition (Acton 1978). Therefore, if optically thin emission does not apply, transitions with very different oscillator strength may suffer different attenuation/enhancement, with stronger effects occurring in lines with higher oscillator strengths. In the ratios inspected, the lines with higher oscillator strength are the Lyα line of N VII and O VIII, and the 13.45 Å line of Ne IX (e.g., Testa et al. 2007). Non-negligible optical depth is expected in strong X-ray resonance lines produced from shock-heated plasma in CTTSs (Argiroffi et al. 2009). The observed variable ratios might indicate that some lines are affected by a changing optical depth. Since the expected attenuation/enhancement with respect to optically thin emission depends on the source

geometry and viewing angle, stellar rotation can produce periodic changes in the line opacity, and hence in the observed ratios. However, once again the three ratios do not vary in the same direction, with N VII and O VIII ratios being higher in the *high* state, whereas the ratio of the slightly hotter Ne IX lines is higher in the *low* phase. This is evident from Table 4 and Figure 4.

In summary, we stress the significant variations observed in line ratios between *low* and *high* phases. The origin of these variations remains unclear. If these variations were due to changes in plasma temperature or absorption, a coherent behavior would be expected for the three ratios, and this is not the case. Opacity effects instead can operate in a more complex way, provoking both line enhancements or reductions, depending on the source geometry and viewing angle. This hypothesis is therefore the most intriguing, especially considering that in some phases line ratios are discrepant from the value expected in the optically thin limit.

6. DISCUSSION

The main result of the time-resolved spectral analysis of the X-ray-emitting plasma from V4046 Sgr (Section 5) is that the high-density plasma component at 3–4 MK is rotationally modulated with a period of half the system orbital period, with maximum and minimum phases occurring at quadrature and conjunction epochs, respectively. The observed X-ray rotational modulation indicates that this high-density plasma component is not symmetrically distributed with respect to the stellar rotational axes. We also found that strong emission lines from this plasma component provide some indications of non-negligible optical depth effects, and that the periodic modulation appears to be associated with variations in the source optical depth, as evidenced by the significant variations in line ratios sensitive to optical depth observed between *low* and *high* phases.

The strongest X-ray emission lines, produced by shock-heated material in CTTSs, are expected to have non-negligible optical depth due to the high density and typical size of the post-shock region (Argiroffi et al. 2009). Moreover, the optical depth should vary if the viewing geometry of the post-shock region changes.

Hints of non-negligible optical depth observed in the strongest X-ray lines of V4046 Sgr indicate that the high-density plasma is mostly concentrated in a compact portion of the stellar surface, as predicted for the post-shock material. Moreover, the variability of the optical depth can be naturally explained with the changing viewing geometry of the volume occupied by the high-density plasma during stellar rotation. This scenario requires plasma confinement by the stellar magnetic fields.

We observed an X-ray period of half the system orbital period, as already observed for accretion indicators (e.g., Vrba et al. 1993; Kurosawa et al. 2005) and X-ray emission (Flaccomio et al. 2005) from some CTTSs. That could be explained, in the case of V4046 Sgr, by different scenarios. If the X-ray-emitting plasma is located in only one of the two system components, then a period of half the rotational period is observed when there are two accretion-shock regions on the stellar surface at opposite longitudes, or there is only one accretion-shock region and the maximum X-ray flux is observed when the base of the accretion stream is viewed sideways (Argiroffi et al. 2011, a configuration that occurs twice in one stellar rotation).

Considering the system symmetry and the accretion geometry previously suggested by Stempels & Gahm (2004), it is conceivable that both components possess similar amounts of high-density cool plasma. In this scenario, the half-period can be naturally explained assuming that the location on each stellar surface of this plasma, compact and not azimuthally symmetric with respect to each stellar rotation axis, is symmetric for 180° rotations with respect to the binary rotation axis.

The simultaneous optical monitoring campaign indicated that the two components have similar accretion rates, validating the assumption that the two components possess similar amounts of high-density plasma. However, the optical accretion spots, probed by Ca II IRT, did not show rotational modulation (Donati et al. 2011). Therefore, accretion regions emitting Ca II should be symmetrically distributed with respect to the stellar poles. This scenario, different from that obtained from the X-ray data, could be reconciled considering that X-rays are likely produced only by a fraction of the entire accretion-shock region (Sacco et al. 2010).

In conclusion, our *XMM-Newton*/RGS data of the V4046 Sgr close binary system have shown for the first time the rotational modulation of X-ray lines characteristic of a cool, high-density plasma corotating with the stars. This strongly support the accretion-driven X-ray emission scenario, in which the high-density cool plasma of CTTSs is material heated in the accretion shock. It moreover suggests that the accretion flow is channeled by magnetic field lines anchored on the stars, along small magnetic tubes. This is consistent with the general framework of magnetic accretion, but brings new insights into the accretion mechanism in close binary systems of CTTSs.

This work is based on observations obtained with *XMM-Newton*, an ESA science mission with instruments and contributions directly funded by ESA Member States and NASA. C.A., A.M., and F.D. acknowledge financial contribution from the agreement ASI-INAF I/009/10/0. J.K.'s research on accreting young stars near Earth is supported by National Science Foundation grant AST-1108950 to RIT.

REFERENCES

Acton, L. W. 1978, ApJ, 225, 1069
Argiroffi, C., Flaccomio, E., Bouvier, J., et al. 2011, A&A, 530, A1
Argiroffi, C., Maggio, A., & Peres, G. 2007, A&A, 465, L5
Argiroffi, C., Maggio, A., Peres, G., et al. 2009, A&A, 507, 939
Arnaud, K. A. 1996, in ASP Conf. Ser. 101, Astronomical Data Analysis Software and Systems V, ed. G. H. Jacoby & J. Barnes (San Francisco, CA: ASP), 17
Bouvier, J., Alencar, S. H. P., Harries, T. J., Johns-Krull, C. M., & Romanova, M. M. 2007, Protostars and Planets V (Tucson, AZ: Univ. Arizona Press), 479
Bouvier, J., Cabrit, S., Fernandez, M., Martin, E. L., & Matthews, J. M. 1993, A&A, 272, 176
Brickhouse, N. S., Cranmer, S. R., Dupree, A. K., Luna, G. J. M., & Wolk, S. 2010, ApJ, 710, 1835
Curran, R. L., Argiroffi, C., Sacco, G. G., et al. 2011, A&A, 526, A104
de Val-Borro, M., Gahm, G. F., Stempels, H. C., & Pepliński, A. 2011, MNRAS, 413, 2679
Donati, J.-F., Gregory, S. G., Montmerle, T., et al. 2011, MNRAS, 417, 1747
Donati, J.-F., Skell, M. B., Bouvier, J., et al. 2010, MNRAS, 409, 1347
Drake, J. J., Testa, P., & Hartmann, L. 2005, ApJ, 627, L149
Dupree, A. K., Brickhouse, N. S., Cranmer, S. R., et al. 2012, ApJ, 750, 73
Ercolano, B., Drake, J. J., Raymond, J. C., & Clarke, C. C. 2008, ApJ, 688, 398
Favata, F., & Micela, G. 2003, Space Sci. Rev., 108, 577
Feigelson, E. D., & Montmerle, T. 1999, ARA&A, 37, 363
Flaccomio, E., Micela, G., Sciortino, S., et al. 2005, ApJS, 160, 450
Gorti, U., & Hollenbach, D. 2009, ApJ, 690, 1539
Güdel, M., & Nazé, Y. 2009, A&AR, 17, 309
Güdel, M., Skinner, S. L., Mel'Nikov, S. Y., et al. 2007, A&A, 468, 529
Güdel, M., & Telleschi, A. 2007, A&A, 474, L25
Gullbring, E. 1994, A&A, 287, 131

Günther, H. M., Liefke, C., Schmitt, J. H. M. M., Robrade, J., & Ness, J. 2006, A&A, 459, L29
Günther, H. M., Schmitt, J. H. M. M., Robrade, J., & Liefke, C. 2007, A&A, 466, 1111
Hartmann, L., Hewett, R., & Calvet, N. 1994, ApJ, 426, 669
Herbst, W., Herbst, D. K., Grossman, E. J., & Weinstein, D. 1994, AJ, 108, 1906
Huenemoerder, D. P., Kastner, J. H., Testa, P., Schulz, N. S., & Weintraub, D. A. 2007, ApJ, 671, 592
Kashyap, V., & Drake, J. J. 2000, Bull. Astron. Soc. India, 28, 475
Kastner, J. H., Huenemoerder, D. P., Schulz, N. S., Canizares, C. R., & Weintraub, D. A. 2002, ApJ, 567, 434
Kastner, J. H., Sacco, G. G., Montez, R., et al. 2011, ApJ, 740, L17
Kastner, J. H., Zuckerman, B., Hily-Blant, P., & Forveille, T. 2008, A&A, 492, 469
Königl, A. 1991, ApJ, 370, L39
Kurosawa, R., Harries, T. J., & Symington, N. H. 2005, MNRAS, 358, 671
Lamzin, S. A. 1999, Astron. Lett., 25, 430
Ness, J., Güdel, M., Schmitt, J. H. M. M., Audard, M., & Telleschi, A. 2004, A&A, 427, 667
Petrov, P. P., Gahm, G. F., Gameiro, J. F., et al. 2001, A&A, 369, 993
Preibisch, T., Kim, Y., Favata, F., et al. 2005, ApJS, 160, 401
Robrade, J., & Schmitt, J. H. M. M. 2007, A&A, 473, 229
Rodriguez, D. R., Kastner, J. H., Wilner, D., & Qi, C. 2010, ApJ, 720, 1684
Sacco, G. G., Argiroffi, C., Orlando, S., et al. 2008, A&A, 491, L17
Sacco, G. G., Orlando, S., Argiroffi, C., et al. 2010, A&A, 522, A55
Schmitt, J. H. M. M., Robrade, J., Ness, J., Favata, F., & Stelzer, B. 2005, A&A, 432, L35
Stempels, H. C., & Gahm, G. F. 2004, A&A, 421, 1159
Testa, P., Drake, J. J., & Peres, G. 2004, ApJ, 617, 508
Testa, P., Drake, J. J., Peres, G., & Huenemoerder, D. P. 2007, ApJ, 665, 1349
Torres, C. A. O., Quast, G. R., Melo, C. H. F., & Sterzik, M. F. 2008, in Handbook of Star Forming Regions: Volume II, The Southern Sky, ed. B. Reipurth (San Francisco, CA: ASP), 757
Ulrich, R. K. 1976, ApJ, 210, 377
Vrba, F. J., Chugainov, P. F., Weaver, W. B., & Stauffer, J. S. 1993, AJ, 106, 1608
Wilms, J., Allen, A., & McCray, R. 2000, ApJ, 542, 914